



PII: S0017-9310(96)00205-0

Spectral optical functions of silicon in the range of 1.13–4.96 eV at elevated temperatures

BYUNG K. SUN,† XIANG ZHANG and COSTAS P. GRIGOROPOULOS‡

Department of Mechanical Engineering, University of California, Berkeley, CA 94720, U.S.A.

(Received 22 January 1996 and in final form 31 May 1996)

Abstract—This work presents an experimental procedure for measuring high temperature spectral optical functions of materials. The complex refractive index is determined over a spectral range of 1.13–4.96 eV at high temperatures by ellipsometry in a reduced pressure, inert gas environment. On the basis of the measured complex refractive index, relevant optical functions such as the complex dielectric function, normal incidence reflectance, and absorption coefficient are also obtained. Silicon is selected due to the fact that, even though it has numerous applications in microelectronics fabrication and processing, the available spectral optical property data are incomplete at high temperatures. The experimental results are compared with the existing published data. Copyright © 1996 Elsevier Science Ltd.

1. INTRODUCTION

Silicon is extensively used as a substrate or constructing material for manufacturing microelectronic devices or packages such as VLSI, MCM-D, AM-LCD, solar cells, etc. Processing of silicon in various electronic manufacturing environments usually involves rigorous temperature or thermal energy management which in turn requires *in situ* non-disruptive temperature measurement techniques to implement successful process control. Despite their importance, few *in situ* temperature measurements have been reported for microelectronic device fabrication processes. The development of non-disruptive measurement techniques has been limited by lack of data on the material properties or optical functions at elevated temperatures. In addition, accurate knowledge of the radiative properties of silicon at high temperatures is important for many applications including laser micromachining, laser ablation, thin film deposition, melting-model calculations of pulsed laser annealing and concentrator solar cell applications, which ask for systematic understanding of interaction phenomena between the incident light and the solid surface.

A frequently adopted technique for evaluating the optical properties of bulk materials and thin films is ellipsometry, which correlates the polarization change of light upon reflection with the optical properties of the material [1, 2]. Meulen and Hien measured the complex refractive index of bulk silicon up to 1350 K at a fixed wavelength, $\lambda = 632.8$ nm (He-Ne laser

line), using an automatic ellipsometer [3]. Algazin *et al.* reported the complex refractive index of atomically pure silicon surfaces, measured by ellipsometry at a wavelength, $\lambda = 632.8$ nm, from room temperature to a temperature close to the melting point of silicon, $T_m = 1685$ K [4]. Jellison *et al.* experimentally measured, with polarization modulation ellipsometry, and presented the spectroscopic temperature dependence of optical functions of bulk silicon between 1.6 and 4.7 eV ($\lambda = 0.264$ – 0.770 μm), for temperature up to 1023 K [5–7]. Recently, Xu and Grigoropoulos presented data on the optical constants of bulk silicon and polysilicon using null ellipsometry at the $\lambda = 632.8$ nm wavelength up to a temperature of 1400 K [8]. Though many investigators have contributed measurements of temperature dependent optical constants of silicon, experimental data are still scarce for temperatures higher than about 1000 K.

The present work is designed to measure the optical properties, the complex refractive index \tilde{n} of microelectronic grade pure single crystalline silicon, by a scanning automatic ellipsometer. Subsequently, the normal incidence reflectivity, R , the complex dielectric function, $\tilde{\epsilon}$, and absorption coefficient, α , are deduced from the measured complex refractive index. Extension of the temperature range for ellipsometric measurement of the optical constants of material up to 1527 K over a spectral range of 480–1100 nm wavelength and up to 1183 K over a spectral range of 250–480 nm, respectively, is sought. The experimental results are compared with most recently available data. A simple and efficient experimental procedure is implemented to minimize the effects of the thermal emission from the sample [6] and of background radiation. These effects have reportedly hindered accurate

† Visiting Research Associate, R & D Center, SAMSUNG ELECTROMECHANICS CO., LTD., Suwon, Korea.

‡ Author to whom correspondence should be addressed.

NOMENCLATURE

a_n	fitting constant for the temperature dependence of the real part of the complex refractive index— temperature coefficient of the refractive index	V	total number of experimental observations
a_k	fitting constant for the temperature dependence of the imaginary part of the complex refractive index— temperature coefficient of the extinction constant	W	number of fit parameters.
a_R	fitting constant for the temperature dependence of the normal incidence reflectivity—temperature coefficient of the normal incidence reflectivity	Greek symbols	
d	layer thickness	Δ	phase difference between the TE and TM waves
i	$\sqrt{-1}$	$\bar{\epsilon}$	complex dielectric function ($\epsilon_1 + i\epsilon_2$)
h	Planck's constant	ϵ_1	real part of the complex dielectric function
k	imaginary part of the complex refractive index—extinction coefficient	ϵ_2	imaginary part of the complex dielectric function
M	characteristic transmission matrix of a single layer	θ	angle of refraction in the oxide layer (θ_{ox}) or the silicon wafer (θ_{c-si})
MSE	mean square error function defined by equation (5)	θ_i	ellipsometric beam angle of incidence with respect to the sample surface
n	real part of the complex refractive index—refractive index	λ	light wavelength
n_0	refractive index at the fitting reference temperature	ν	light frequency
\tilde{n}	complex refractive index ($n + ik$)	ρ	ratio of Fresnel reflection coefficients for the TE and TM polarized waves
p	characteristic matrix parameter	σ	measured standard deviation of the ellipsometric measurement
R	normal incidence reflectivity	ψ	arctangent of magnitude of ρ .
r	Fresnel reflection coefficient	Subscripts	
T	temperature	c	calculated result
T_0	reference temperature for fitting	c-Si	crystalline silicon
		j	notation for p or s polarization
		m	measured result
		ox	thermally oxidized layer on bulk crystalline silicon
		p	TM wave
		s	TE wave.

measurement of bulk silicon optical properties at temperatures higher than 1000 K.

2. EXPERIMENTAL PROCEDURES

The sample examined in this study was a pure single crystalline silicon wafer having a thermally grown oxide layer. The oxide layer thickness is in the neighborhood of 1200 Å, and was thermally grown by setting the oxidation temperature and controlling the reaction time. The sample wafer was pre-cleaned by standard gate-oxide procedures, and all processing was done on equipment routinely used for the production of high quality gate oxides.

All measurements must be carried out in a high vacuum inert environment to avoid detrimental effects of oxide growth at elevated temperatures on the accuracy of measured data. A special custom-designed stainless steel chamber of 14 in. diameter, equipped with two rotary pumps and a turbo-molecular pump,

was constructed for this purpose (Fig. 1). Before heating the sample, the chamber was evacuated to a pressure of 10^{-2} torr and refilled with pure argon gas. After argon flushing, the chamber was re-evacuated to a pressure of 10^{-5} torr. The chamber is also equipped with three pairs of entrance-exit windows, with azimuthal angles of 39° , 70° and 75° to accommodate ellipsometric and photometric measurements at different angles. The windows are made of special stress-free glass to minimize undesirable window effects on the measurement [3]. The entire chamber was water cooled to avoid any thermal expansion or damage to the chamber due to high temperature radiation heat transfer from the sample holding graphite.

A 2.5 kW induction heating unit generates high frequency current in the graphite susceptor through an induction heating coil. The temperature of the silicon sample can be raised to 1400°C. The sample is mounted to the graphite susceptor by air-setting high temperature cement to establish complete and uniform

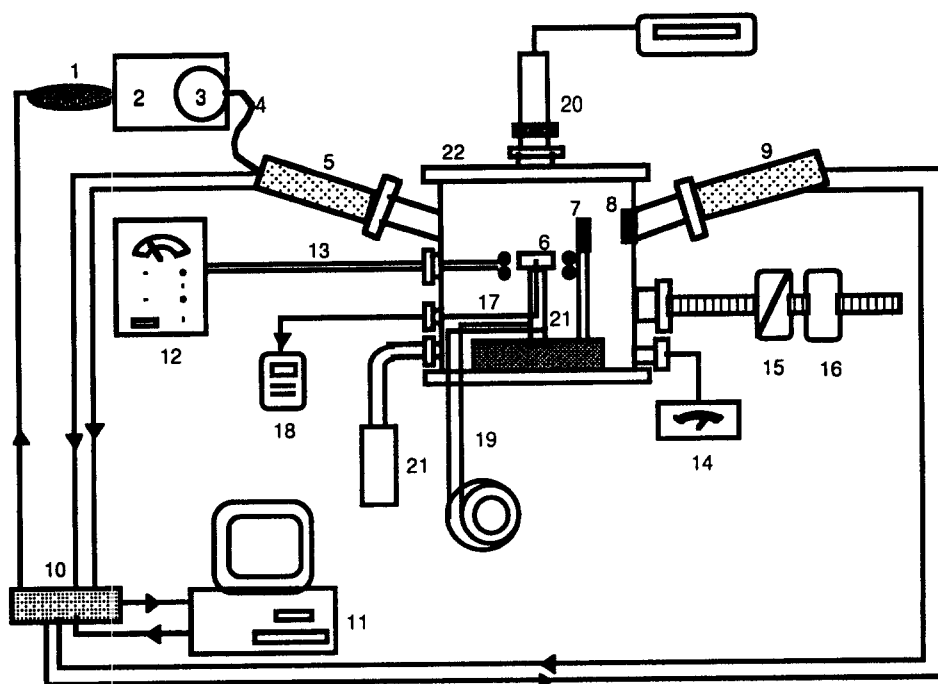


Fig. 1. Experimental set-up for high temperature optical refractive index measurement.

- | | |
|---|------------------------------------|
| 1. Xenon short arc lamp | 12. Induction heating power supply |
| 2. Monochromator | 13. Induction coil |
| 3. Filter/chopper unit | 14. Pressure gauge |
| 4. Optical fiber | 15. Two rotary mechanical pumps |
| 5. Polarizer unit | 16. Turbo-molecular pump |
| 6. Sample holding stage (graphite) | 17. Thermocouple |
| 7. Fine aperture | 18. Digital thermometer panel |
| 8. Coarse aperture | 19. Cooling water feed-through |
| 9. Analyzer unit | 20. Infra-red pyrometer |
| 10. Power/control box | 21. Argon gas cylinder |
| 11. Personal computer for system control and data acquisition | 22. Chamber |

contact between the susceptor and the sample. Notably, the graphite susceptor block provides a self-sustaining reducing environment at high temperatures by supplying trace CO (reducing) or CO₂ (neutral) gas through combining with residual oxygen, if any, in the chamber. The susceptor block is supported by a ceramic pole that is cooled by continuous water flow. The position and orientation of the sample are manually controlled by several control screws. On the basis of experimental findings in this study, serious consideration should be taken to maintain stability of the sample holding block at elevated temperatures. Even minimal slip of any of the various components associated with the sample holding block due to a temperature rise can completely disturb the optical alignment at elevated temperatures. The temperature of the sample was determined by a factory-calibrated chromel-alumel (K-type) thermocouple that was embedded in the center of the graphite susceptor and its relative validity was continuously monitored by an I.R. pyrometer during measurements. The error of the thermocouple calibration is less than 2°C.

A spectroscopic rotating-analyzer ellipsometer

(RAE) (J. A. Woollam Co.) was used for these measurements. Basic concepts and details of RAE have been discussed elsewhere [1, 3, 9, 18]. Briefly, the ellipsometer source is a 75 W xenon short arc lamp, operating in the spectral range of 200–2000 nm, equipped with a fused silica collimating lens. The monochromator has several grating options, and includes an integrated optical chopper. The polarizer is a calcite Glan–Taylor ultraviolet-transmitting prism type. The analyzer is rotatable by a computer-driven synchronous stepper motor and is optically the same element as the fixed polarizer. A silicon photo-detector is mounted on the optical axis behind the hollow shaft stepper motor. System control and data acquisition are performed by a personal computer.

The components of the RAE are installed in the chamber, as shown in Fig. 2. The broadband light generated by the Xenon short arc lamp is focused onto the monochromator entrance slit by an ellipsoidal reflector. The reflected light passes through the monochromator whose grating angle is adjusted via a computer controlled stepper motor. The light is transferred by an optical fiber cable to the filter/chopper

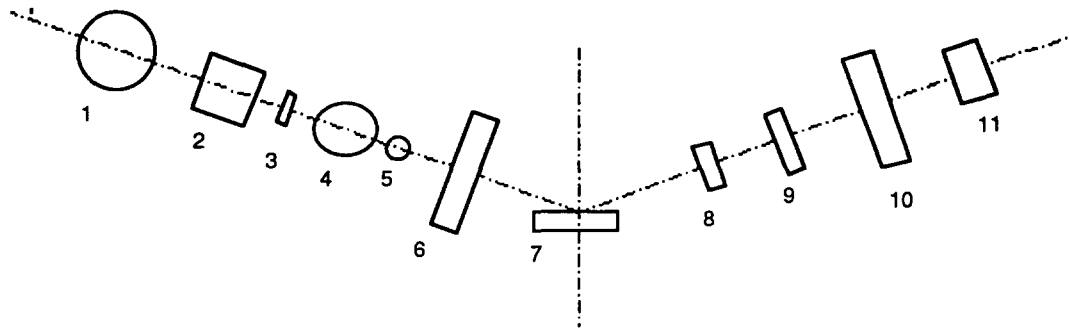


Fig. 2. Schematic of the ellipsometric optical arrangement.

- | | |
|------------------|--------------------|
| 1. Light source | 7. Sample surface |
| 2. Monochromator | 8. Fine aperture |
| 3. Filter | 9. Coarse aperture |
| 4. Chopper | 10. Analyzer |
| 5. Collimator | 11. Photo-detector |
| 6. Polarizer | |

unit. The signal-to-noise ratio of the sampled analog signal is thus improved by reducing the sensitivity to changes in the ambient light level. The signal filtering electronic unit is tuned to the chopping frequency. The light is then collimated by a fixed 33 mm focal length quartz lens and polarized by the Glan–Taylor type prism polarizer, which is mounted on a stepper-driven rotational stage. The accuracy of this stage is better than 0.01° . The incident light passing through an iris exit diaphragm is reflected on the sample surface with a resulting polarization change. The reflected light again passes through two consecutive apertures and an iris diaphragm attached to the analyzer unit.

The first aperture of an adjustable diameter from 0.02 to 10 mm is installed at a distance of about 7 cm from the center of the measured sample area, and the second aperture of a fixed diameter, 10 mm, is mounted on the interior wall of the chamber. The first aperture prevents the strong direct thermal emission of the sample and the graphite stage from entering the analyzer unit and the second reduces the amount of reflected stray light entering the analyzer unit. The diameter of the first aperture should be adjusted to a smaller size than that of the probing light beam, to successfully perform ellipsometric measurements at temperatures higher than 700°C , by isolating the direct emission from the graphite sample stage. With the aid of these apertures and the optical chopper mentioned above, the measurements were carried out at high temperatures. No meaningful data could be obtained at temperatures higher than 700°C without the aperture set-up. Especially, in the case of near-uv or uv spectral range, even with the aid of the above mentioned set of apertures, measurements at temperatures higher than approximately 910°C become statistically meaningless due to significantly reduced signal to noise ratio, which results from detrimental combination of reduced intensity of the xenon lamp in the uv spectral range, reduced uv throughput of the

system, and strong irregular background emission from the graphite susceptor block.

From the periodic variations of the incident light flux transmitted by the rotating analyzer, detected by the photo-detector, the parameters that describe the reflected polarization ellipse are derived. The instantaneous azimuth of the analyzer is detected by an optical angular encoder. The encoder output provides a synchronizing pulse for each complete rotation. These pulses trigger an analog–digital (A/D) converter which converts the analog signal from the photo-detector to digital form, which is in turn read by an on-line personal computer. The digital intensity data at equi-spaced angular positions of the rotating analyzer are subsequently Fourier analyzed to determine, using least-squares fitting, the polarization state of the reflected light in terms of the ellipsometric angles, ψ and Δ (Section 3, below). With information concerning the incident polarization and the optical model of the sample surface including all known optical parameters, the unknown optical constants of the sample are calculated by iterative regression fitting, using the Marquardt–Levenberg algorithm [10].

3. OPTICS FOR MEASUREMENTS

The state of light polarization is determined by evaluating the relative amplitude and phase difference between the transverse electric wave (TE wave) and the transverse magnetic wave (TM wave) components of the electromagnetic vector field. The ratio, ρ , of the complex reflection coefficient for TM polarized wave, r_p , to the complex coefficient for TE polarized wave, r_s , in terms of the ellipsometric angles ψ , Δ , is given as follows:

$$\rho = r_p/r_s = \tan \psi \exp(i\Delta) \quad 0 \leq \psi \leq \pi/2 \quad 0 \leq \Delta \leq 2\pi. \quad (1)$$

The above expression defines the ellipsometric angle Δ as the change in phase difference and the angle ψ as the arctangent of the magnitude of ρ , which is complex. The characteristic transmission matrix method [11] is used to calculate the reflection coefficients, r_p and r_s . The characteristic matrix for TE polarized wave propagation, $M_{\text{ox},s}$, representing a layer of thickness d_{ox} and having a complex refractive index, \tilde{n}_{ox} is calculated as:

$$M_{\text{ox},s} = \begin{pmatrix} \cos\left(\frac{2\pi}{\lambda} n_{\text{ox}} d_{\text{ox}} \cos \theta_{\text{ox}}\right) & \\ -i n_{\text{ox}} \cos \theta_{\text{ox}} \sin\left(\frac{2\pi}{\lambda} n_{\text{ox}} d_{\text{ox}} \cos \theta_{\text{ox}}\right) & \\ -\frac{i}{n_{\text{ox}} \cos \theta_{\text{ox}}} \sin\left(\frac{2\pi}{\lambda} n_{\text{ox}} d_{\text{ox}} \cos \theta_{\text{ox}}\right) & \\ \cos\left(\frac{2\pi}{\lambda} n_{\text{ox}} d_{\text{ox}} \cos \theta_{\text{ox}}\right) & \end{pmatrix}. \quad (2a)$$

For the TM wave, the characteristic matrix, $M_{\text{ox},p}$, is:

$$M_{\text{ox},p} = \begin{pmatrix} \cos\left(\frac{2\pi}{\lambda} n_{\text{ox}} d_{\text{ox}} \cos \theta_{\text{ox}}\right) & \\ -\frac{i \cos \theta_{\text{ox}}}{n_{\text{ox}}} \sin\left(\frac{2\pi}{\lambda} n_{\text{ox}} d_{\text{ox}} \cos \theta_{\text{ox}}\right) & \\ -\frac{i n_{\text{ox}}}{\cos \theta_{\text{ox}}} \sin\left(\frac{2\pi}{\lambda} n_{\text{ox}} d_{\text{ox}} \cos \theta_{\text{ox}}\right) & \\ \cos\left(\frac{2\pi}{\lambda} n_{\text{ox}} d_{\text{ox}} \cos \theta_{\text{ox}}\right) & \end{pmatrix}. \quad (2b)$$

In the above, λ is the wavelength of the incident light in air. The angle θ_{ox} is found from Snell's law:

$$n_{\text{ox}} \sin \theta_{\text{ox}} = \sin \theta, \quad (3)$$

where θ , is the ellipsometric beam angle of incidence with respect to the sample surface. The reflection coefficient, r_j , is calculated as:

$$r_j = \frac{\begin{pmatrix} (M_{\text{ox},j}(1,1) + M_{\text{ox},j}(1,2)p_{\text{c-Si}}) \\ - (M_{\text{ox},j}(2,1) + M_{\text{ox},j}(2,2)p_{\text{c-Si}}) \end{pmatrix}}{\begin{pmatrix} (M_{\text{ox},j}(1,1) + M_{\text{ox},j}(1,2)p_{\text{c-Si}}) \\ + (M_{\text{ox},j}(2,1) + M_{\text{ox},j}(2,2)p_{\text{c-Si}}) \end{pmatrix}} \quad (4)$$

where $j = p$ or s , $p_{\text{c-Si}} = \tilde{n}_{\text{c-Si}} \cos \theta_{\text{c-Si}}$ for a TE wave, $p_{\text{c-Si}} = 1/(\tilde{n}_{\text{c-Si}}) \cos \theta_{\text{c-Si}}$ for a TM wave and $\tilde{n}_{\text{c-Si}} \sin \theta_{\text{c-Si}} = \sin \theta$.

The ellipsometric angles, ψ and Δ , are calculated from the reflection for the TE and TM waves, using equations (1)–(4). They are used to determine two parameters: the real and imaginary parts of the silicon complex refractive index, n and k . For each combination of parameters, (n, k) , the values, ψ_c and Δ_c are calculated using equation (1) and compared to the corresponding measured values, ψ_m and Δ_m . The set of (n, k) which minimizes the following mean square error function (MSE) is taken as solution:

MSE =

$$\sqrt{\frac{1}{V-W} \sum_i \left[\left(\frac{\psi_{i_c} - \psi_{i_m}}{\sigma_{\psi}} \right)^2 + \left(\frac{\Delta_{i_c} - \Delta_{i_m}}{\sigma_{\Delta}} \right)^2 \right]}. \quad (5)$$

In the above formula, V is the total of number experimental observations (for ellipsometric measurements, there are two observations, ψ and Δ , for each data point), W is the number of fit parameters, σ is the measured standard deviation of the measurement, and the index i is used to indicate summation over all measurements.

The light polarization can be also influenced by the structure and properties of the SiO_2 -Si interface, which is considered as a transition region between the Si and SiO_2 . The existence of a transition region with a thickness of $\sim 7 \text{ \AA}$ has been deduced by other investigators from ellipsometry measurements [12, 13]. However, the effect of the assumed transition region on the measurement results has been found to be insignificant [8]. Therefore, a distinct-sharp interface is assumed to model a simple SiO_2 -Si structure for the determination of the optical properties.

4. EXPERIMENTAL RESULTS

The complex refractive index of crystalline silicon was measured over a spectral range of 250–1100 nm (uv–vis–ir) at temperatures upto 1527 K, depending on the spectral range. A single crystalline silicon wafer with a thermally grown oxide layer was used for the measurements. The thickness and refractive index of the thermally grown oxide were obtained at $\lambda = 632.8 \text{ nm}$ by an automatic ellipsometer with a known incidence angle of 70.0° and an accuracy of 0.01° on ψ and Δ . Using the value $\tilde{n}_{\text{c-Si}} = 3.88 + 0.02i$ [7] for the room temperature complex refractive index of single crystalline silicon, the thickness and refractive index of the thermally grown oxide layer were determined to be 1204 \AA and 1.461 , respectively. With the above obtained information, the silicon sample was then measured at room temperature on the apparatus described in the previous section to determine the 'true' angle of incidence. The refractive index and temperature coefficient of SiO_2 , given by Malitson [14] were used for spectral measurements. In addition, the thermal expansion effect of the oxide layer was taken into account by taking the SiO_2 thermal expansion rate of $5 \times 10^{-7} \text{ \AA \AA}^{-1} \text{ }^\circ\text{C}^{-1}$ [15]. The samples were used for only one heating-cooling cycle, and no significant additional oxide was detected by room temperature measurements after the heating-cooling cycle. A three-phase model (air–silicon oxide–silicon) was used to interpret the ellipsometric angles, ψ and Δ , in terms of the refractive index (n) and extinction coefficient (k) of silicon.

The spectroscopic data of the measured components of the silicon refractive index, n and extinction

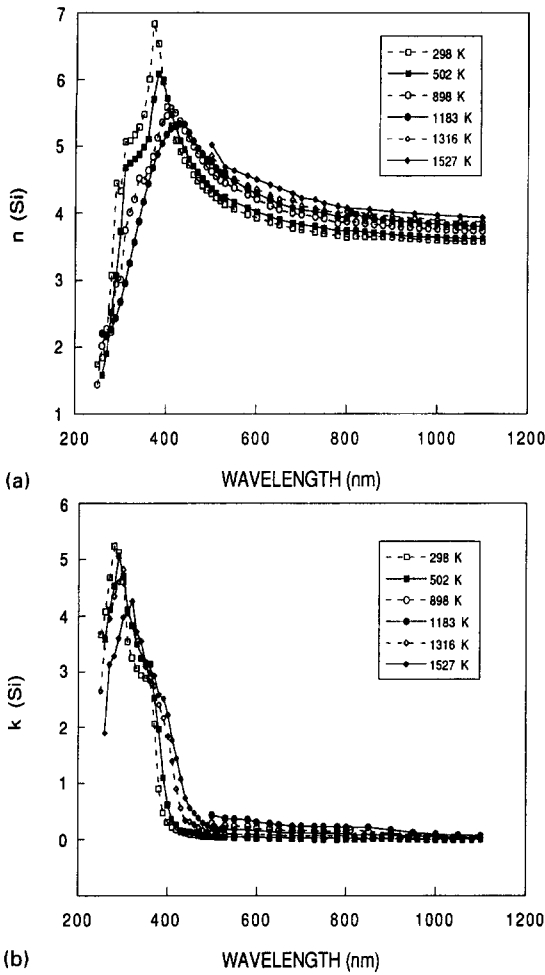


Fig. 3. Spectral temperature dependence (a) of the refractive index, n , of pure single crystalline silicon; (b) of the extinction coefficient, k of pure single crystalline silicon.

coefficient, k are shown in Fig. 3(a) and (b), respectively, for selected temperatures as indicated. The temperature dependence of both the refractive index and the extinction coefficient is confirmed by these measurements and is found to be valid in the extended temperature range and over the spectral range of 480–1100 nm. Spectral measurement errors in the refractive index, n , and the extinction coefficient, k are statistically determined and shown in Fig. 4. The errors are based on a 90% confidence level over the entire spectral range of this experiment. Detailed discussion of measurement accuracy or uncertainty of the rotating analyzer ellipsometers can be found elsewhere [2, 14].

Comparisons between these measurements and other published results [7, 8] are shown in Figs. 5 and 6. The spectral data of n shown in Fig. 5 indicate that the results of these measurements compare well with other data [7]. The agreement is within 5%, in general, even though there seems to be some deviation of the measured values from the published ones for the spectral range of 480–500 nm at higher temperatures such

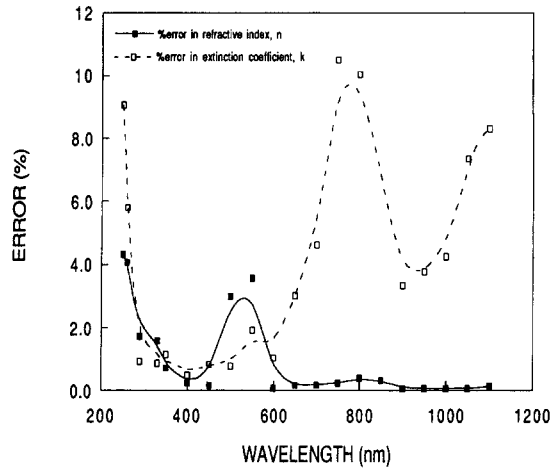


Fig. 4. Spectral measurement errors in refractive index and extinction coefficient.

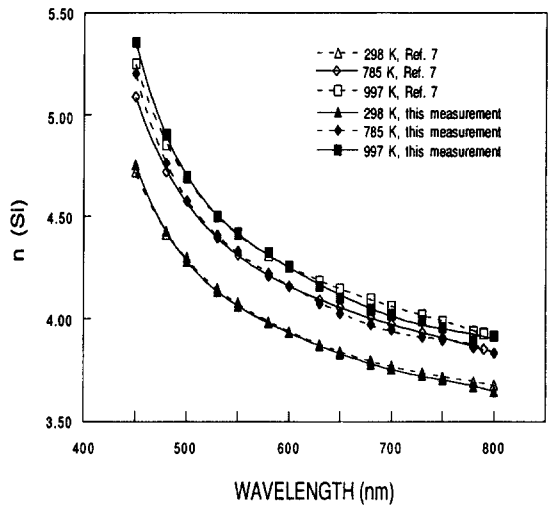


Fig. 5. Comparison between the measured and the published complex refractive index, n , data for selected temperatures.

as 785 and 997 K. The temperature dependent data at the He–Ne laser line, 632.8 nm, shown in Fig. 6, also compare well with the published data [8].

It was experimentally found that n and k were a linear function and an exponential function of temperature, respectively, from 298 to 1023 K at all wavelengths above 450 nm; the coefficients of the linear and exponential terms were functions of wavelength [6–8]. The following expressions are obtained:

$$n(\lambda, T) = n_0(\lambda) + a_n(\lambda)(T - T_{0n}) \quad (6)$$

$$k(\lambda, T) = a_k(\lambda) \exp(T/T_{0k}) \quad (7)$$

where T_{0n} , T_{0k} are the reference temperatures for fitting. In these measurements, $T_{0n} = 25^\circ\text{C}$ was used for the refractive index and $T_{0k} = 498^\circ\text{C}$ for the extinction coefficient. The fitted values of $a_n(\lambda)$ and $a_k(\lambda)$ are shown together with the published data [7] in Figs. 7 and 8. These measurement results comprise the data collected from the extended temperature range of

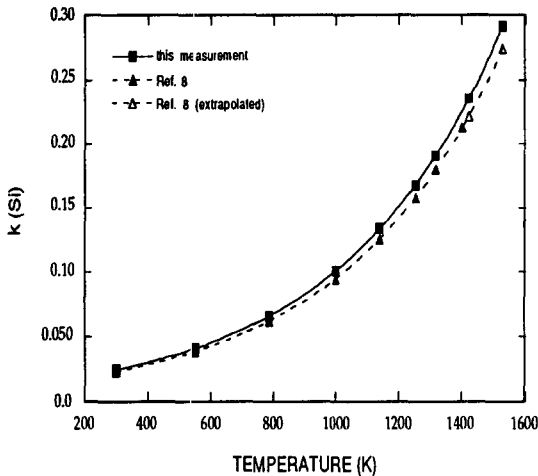
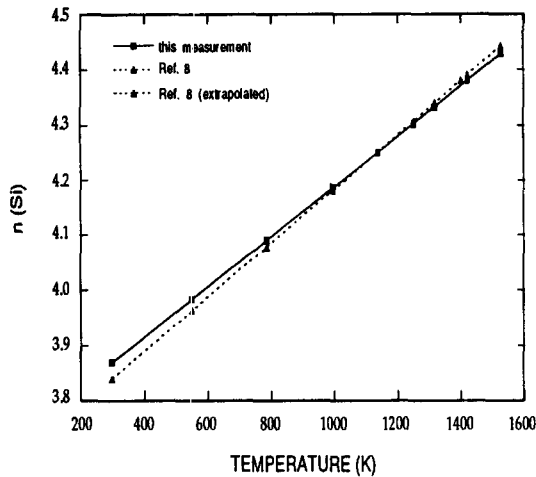


Fig. 6. Comparison between the measured and the published complex refractive index (n and k) for the He-Ne laser line, $\lambda = 632.8$ nm (data have been generated from fitting parameters for both the measured and the published index).

1024–1527 K, which the published data did not cover. However, it is noticed the polynomial for $a_n(\lambda)$ presented in ref. [7] does not properly describe the experimental data shown in that publication. Thus, given that the deduction of k by reverse calculations from known n and R (normal incidence reflectivity) is very sensitive to variations in n , the spectral fitting function, $a_k(\lambda)$, could not be derived from that publication's data for comparison.

The normal incidence reflectivity is calculated from the following expression:

$$R(\lambda, T) = [(n-1)^2 + k^2] / [(n+1)^2 + k^2]. \quad (8)$$

The normal incidence reflectivity is, to a good approximation, also a linear function of temperature in the spectral range of 480–1100 nm given by:

$$R(\lambda, T) = R_0(\lambda) + a_R(\lambda)(T - T_{OR}) \quad (9)$$

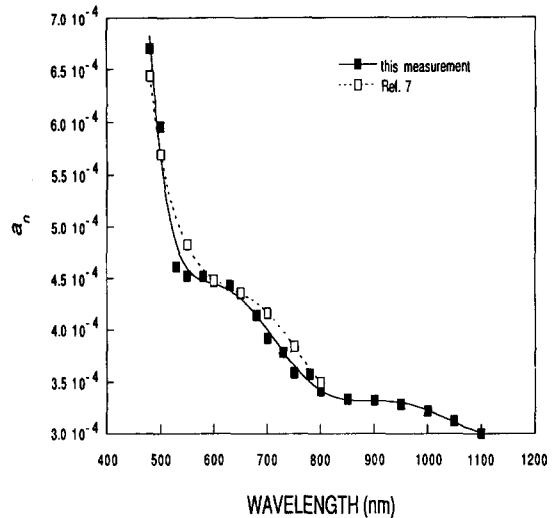


Fig. 7. Spectral temperature coefficient, a_n , of the refractive index of pure single crystalline silicon.

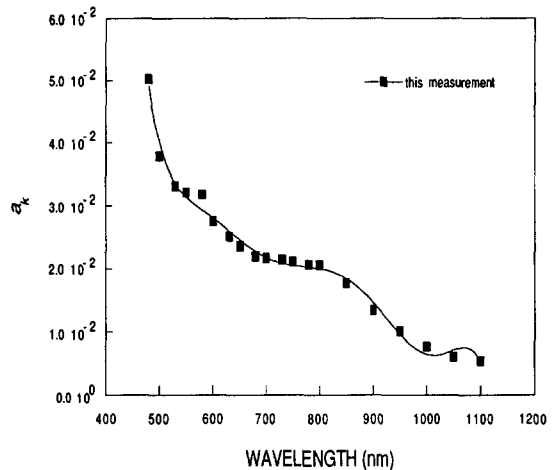


Fig. 8. Spectral temperature coefficient, a_k , of the extinction coefficient of pure crystalline silicon.

where $T_{OR} = 25^\circ\text{C}$, the reference temperature for fitting.

The calculated values of R and a_R using the measured n and k values are shown in Figs. 9 and 10. On the basis of the comparison between the published data and the measurement data, it should be pointed out that the temperature coefficients of both the measured refractive index and the normal incidence reflectivity are somewhat larger and show sharp decays in the spectral range of 480–550 nm than the published data. In all cases, the data have been fitted by seventh-order polynomials in the wavelength (nm). The derived coefficients and estimated fitting errors are summarized in Table 1.

The normal incidence reflectivity data of this experiment are shown together with data published in ref. [6] in Fig. 11. They are quite compatible with each other. It can be seen that the peak in R which is located near 3.4 eV at 10 K moves to lower energies with

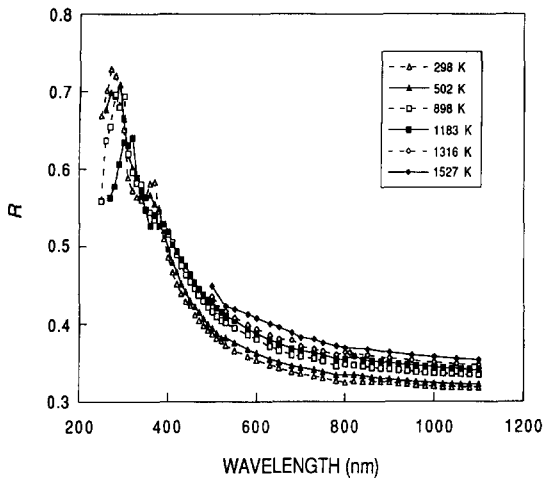


Fig. 9. Spectral temperature dependence of the normal incidence reflectivity, R , of pure crystalline silicon.

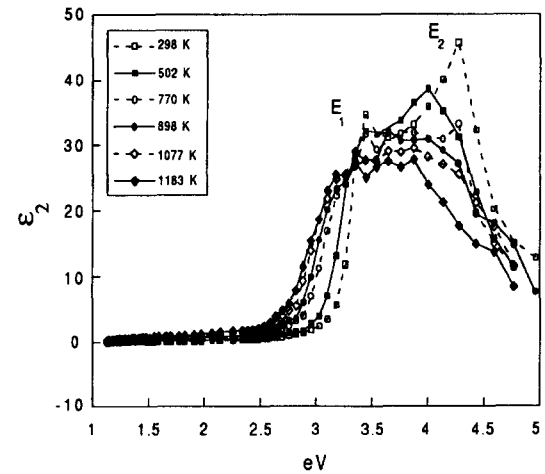
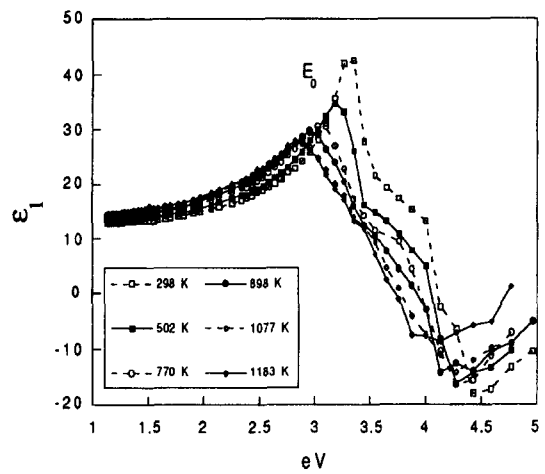


Fig. 12. Spectral temperature dependence of the complex dielectric function, $\tilde{\epsilon}(\epsilon_1 + i\epsilon_2)$ of pure single crystalline silicon.

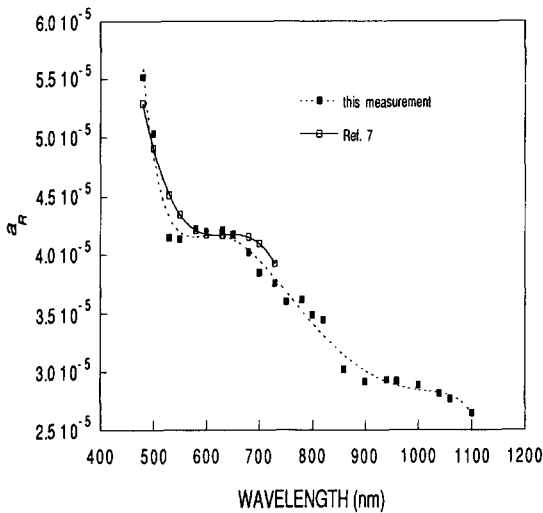


Fig. 10. Spectral temperature coefficient, a_R , of the normal incidence reflectivity of pure single crystalline silicon.

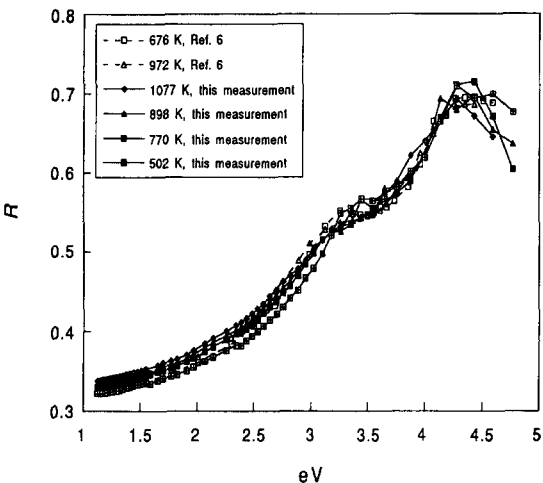


Fig. 11. Comparison of the spectral normal reflectivity data of this measurement and ref. [6].

increasing temperature, and disappears around 500°C. Above 500°C, R is a monotonically increasing function of energy from 2–4 eV. Below ~ 3 eV, R increases linearly with temperature as shown in equation (9).

The complex dielectric function, $\tilde{\epsilon}(\epsilon_1 + i\epsilon_2)$ and the absorption coefficient, α , are expressed by the following relations, respectively:

$$\epsilon_1 = n^2 - k^2 \quad \text{and} \quad \epsilon_2 = 2nk \quad (10)$$

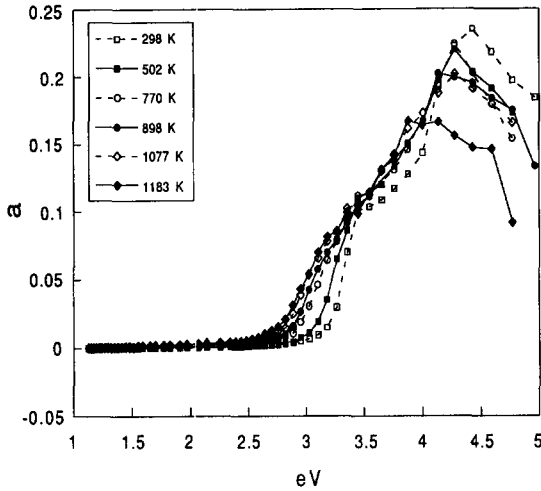
$$\alpha = 4\pi k/\lambda. \quad (11)$$

The corresponding spectral data for higher temperatures are also shown in Figs. 12 and 13, respectively. From Fig. 12, the same features observed in ref. [6] are apparent, even for the extended temperature ranges up to 1183 K. Briefly, the peak in ϵ_1 near 3.4 eV keeps decreasing in magnitude, moves to lower energy and broadens as the temperatures increases. It clearly appears in the ϵ_1 spectra as a low-energy cut-

Table 1. The coefficients to the seventh-order polynomial fits shown in Figs. 7, 8 and 10

Coefficient	a_n	a_k	a_R
$A(0)$	0.33588813	52.35726919	0.02183606
$A(1)$	-0.00294738	-0.49677648	-0.00019230
$A(2)$	$1.09429183 \times 10^{-5}$	0.00199993	$7.18770301 \times 10^{-7}$
$A(3)$	$-2.22514782 \times 10^{-8}$	$-4.42216155 \times 10^{-6}$	$-1.47666339 \times 10^{-9}$
$A(4)$	$2.67703630 \times 10^{-11}$	$5.79704820 \times 10^{-9}$	$1.80290962 \times 10^{-12}$
$A(5)$	$-1.9067134 \times 10^{-14}$	$-4.50414494 \times 10^{-12}$	$-1.30987029 \times 10^{-15}$
$A(6)$	$7.45012106 \times 10^{-18}$	$1.92037226 \times 10^{-15}$	$5.24940655 \times 10^{-19}$
$A(7)$	$-1.23293406 \times 10^{-21}$	$-3.46617813 \times 10^{-19}$	$-8.95987800 \times 10^{-23}$
Fitting error	0.530%	0.450%	0.675%

$$a_\pi = A(0) + A(1)\lambda - A(2)\lambda^2 + A(3)\lambda^3 + A(4)\lambda^4 + A(5)\lambda^5 + A(6)\lambda^6 + A(7)\lambda^7 \text{ where } \pi = n, k, R \text{ and } \lambda \text{ is in nm.}$$

Fig. 13. Spectral temperature dependence of the absorption coefficient, α , of pure crystalline silicon.

off shoulder. This peak is labeled by E_0 in Fig. 12 and is considered to arise primarily from a M_0 critical point in the joint density of states for $\Gamma_{25}^v \rightarrow \Gamma_{15}^c$ transition. The critical-point energy for this transition did not occur exactly at the top of the peak but rather at the low-energy side [16].

The peak in ϵ_2 near 4.4 eV also decreases in magnitude and moves to lower energy as the temperature increases. The slope decreases with increasing temperature. This peak in ϵ_2 is identified by E_2 in Fig. 12. Its origin is not clear but it is considered to be due to several critical points, including the transitions $\Sigma_2^v \rightarrow \Sigma_3^c$ [17]. None of these features survive at higher temperatures. The peak in the ϵ_2 spectrum near 3.4 eV decreases in magnitude and moves to lower energy as the temperature is increased, until it is no longer significant at $> 500^\circ\text{C}$. This peak is labeled by E_1 in Fig. 12 and corresponds to either a M_0 or M_1 critical point for $\Lambda_3^v \rightarrow \Lambda_1^c$ [16]. It was also found that the critical-point energy at 10 and 300 K is at a slightly lower energy than the peak position. The disappearance of this peak is probably due to the fact that E_1 moves to lower energies faster than E_0 . Thus, when the E_1 peak shifts to energies lower than the E_0

shoulder, it will become indistinguishable. As a result of these movements, ϵ_2 is nearly independent of temperature from 3.8 to 3.2 eV above 500°C . In addition, as shown in Fig. 12, the features of the ϵ_1 and ϵ_2 spectra become broader as the temperature increases.

It appears from the absorption coefficient spectra in Fig. 13 that $\alpha(\lambda, T)$ also becomes independent of temperatures below a critical wavelength $\lambda_c(T)$, even though λ_c does not move monotonically to a longer wavelength with increasing temperature. However, for photon energies well below 3.4 eV (or well below the E_1 or E_0 features) and temperatures between 298 and 1183 K, it is found that the absorption coefficient, which is related to ϵ_2 , observes the empirical relation [5] as follows:

$$\alpha(\lambda, T) = \alpha_0(\lambda) \exp(T/T_{0\alpha}) \quad (13)$$

where $T_{0\alpha} = 430^\circ\text{C}$ for all photon energies, and the $\alpha_0(\lambda)$ is a function of photon energy or wavelength.

Photo-absorption in semiconductors strongly depends on the interaction between the incident photon flux and the semiconductor electronic structure and lattice dynamics. Due to the collective electronic interaction in crystalline silicon, an electronic indirect band gap of 1.12 eV exists, with the Fermi level usually placed between the conduction band and the valence band. On the other hand, the lattice phonon spectrum is generated by the finite temperature field experienced by the crystalline silicon. Incident photons interact with the crystalline silicon via three routes: photon-phonon interaction, photon-electron interaction (including both conducting and valence electrons), and phonon-electron-photon interaction. Light absorption is essentially a result of these interactions in solid silicon. These interactions are often influenced by each other during the absorption process. As the incident photon energy, $h\nu$, increases, i.e. the wavelength decreases, an increasing number of valence electrons can be excited to the conduction band.

More interestingly, electrons in the deep valence band or the lower valence band surface that are shifted from the center of the $E-k$ diagram can be excited directly to the other conduction band without phonon assisted excitation in case of sufficiently high photon

energies. This phenomenon can be seen in Fig. 13 for all temperatures from 298 to 1183 K. However, the relative decreases in the absorption coefficient are observed for photon energies higher than 4.0 eV, which may be related to the existence of multiple conduction bands in the k -space.

The other important issue in photon absorption is the absorption dependence on temperature. As stated earlier, the nature of the indirect band gap in silicon requires phonon-assisted electron excitation by the photon from the valence band to the conduction band, in order to conserve both energy and momentum. Therefore, the phonon spectrum in silicon at a fixed lattice temperature greatly influences the absorption process. Higher lattice temperature represents higher momentum phonons, thereby helping the excitation of more electrons to different conduction bands in the wavenumber-space. This is consistent with the present experimental observation that the absorption coefficient increases with the lattice temperature elevation, up to 4.0 eV photon energy.

The opposite absorption trend with temperature for photon energies above 4.0 eV was previously discussed. The decrease of the band gap at elevated temperatures also enhances the electron excitation, resulting in a higher absorption coefficient. At very high lattice temperature, direct phonon absorption of photons can be realized. This provides an additional channel for absorption enhancement in crystalline silicon.

5. CONCLUSIONS

Automatic ellipsometric measurements have been used in this work to investigate the spectral radiative properties of pure crystalline silicon at high temperatures. A special apparatus was designed and built for measurement in a reduced inert environment of these properties at elevated temperatures over a spectral width of 250–1100 nm. It has been found that rigorous maintenance of optical alignment and reduction of thermal emission effects are crucial for meaningful measurements at higher temperatures. The present work has extended previously reported measurements to a higher temperature range up to 1527 K.

The complex refractive index of a pure crystalline silicon wafer, having a 1204 Å thick oxide overlayer, was measured and its temperature dependence was confirmed for the spectral range of 480–1100 nm. To a good approximation, the refractive index, n , was found to be a linear function of temperature and the extinction coefficient, k , an exponential function of temperature including temperature range of 1023–1527 K. Normal incidence reflectivity and absorption coefficient also showed similar temperature depen-

dence as the complex refractive index, for the same spectral range. Finally, it should be emphasized that the spectral optical or radiative properties in the visible spectral range can be used for accurately monitoring temperature of pure crystalline silicon because of their distinctive and smooth temperature dependence.

Acknowledgement—Support for this work by the National Science Foundation, under Engineering Research Equipment Grant CTS-9310997, is gratefully acknowledged.

REFERENCES

1. Azzam, R. M. A. and Bashara, N. M., *Ellipsometry and Polarized Light*. North-Holland, Amsterdam, 1977.
2. Riedling, K., *Ellipsometry for Industrial Applications*. Springer-Verlag, Wien, 1988, pp. 40–55.
3. Van der Meulen, Y. J. and Hien, N. C., Design and operation of an automated high-temperature ellipsometer. *Journal of the Optical Society of America*, 1974, **64**, 804–811.
4. Algazin, Y. B. and Blyumkina, N. I., Optical constants and temperature dependencies of atomically pure surfaces of germanium and silicon. *Optical Spectroscopy (USSR)*, 1978, **45**, 183–188.
5. Jellison, G. E. Jr. and Modine, F. A., Optical constants for silicon at 300 and 10K determined from 1.64 to 4.73 eV by ellipsometry. *Journal of Applied Physics*, 1982, **53**(5), 3745–3753.
6. Jellison, G. E. Jr. and Modine, F. A., Optical functions of silicon between 1.7 and 4.7 eV at elevated temperatures. *Physical Review, B*, 1983, **27**, 7466–7472.
7. Jellison, G. E. Jr. and Burke, H. H., The temperature dependence of the refractive index of silicon at elevated temperatures at several laser wavelengths. *Journal of Applied Physics*, 1986, **60**, 841–843.
8. Xu, X. and Grigoropoulos, C. P., High temperature radiative properties of thin film polysilicon films at the $\lambda = 0.6328 \mu\text{m}$ wavelength. *International Journal of Heat and Mass Transfer*, 1993, **36**(17), 4163–4172.
9. Aspnes, D. E., Spectroscopic ellipsometry of solids. In *Optical Properties of Solids New Developments*, ed. B. O. Seraphin, 1976, North-Holland, Amsterdam, pp. 799–846.
10. Draper, N. R. and Smith, H., *Applied Regression Analysis*, 2nd edn. Wiley, New York, 1981.
11. Born, M. and Wolf, E., *Principles of Optics*, 6th edn. Pergamon, Exeter, U.K. 1980, pp. 55–60, 611–624.
12. Aspnes, D. E. and Theeten, J. B., Optical properties of the interface between Si and its thermally grown oxide. *Physical Review Letters*, 1979, **43**, 1046–1050.
13. Taft, E. A. and Cordes, L., *Journal of the Electrochemical Society*, 1979, **126**, 131.
14. Malitson, I. H., Interspecimen comparison of the refractive index of fused silica. *Journal of the Optical Society of America*, 1965, **55**, 1205–1209.
15. Grove, A. S., *Physics and Technology of Semiconductor Devices*. Wiley, New York, 1967, p. 102.
16. Daunois, A. and Aspnes, D. E., Electroreflectance and ellipsometry of silicon from 3 to 6 eV. *Physical Review, B*, 1978, **18**, 1824.
17. Kondo, K. and Moritani, A., Symmetry analysis of the E_2 structures in Si by low-field electroreflectance. *Physical Review, B*, 1977, **15**, 812.
18. Aspnes, D. E., Optimizing precision of rotating-analyzer ellipsometers. *Journal of the Optical Society of America*, 1974, **64**, 639–646.